Ab initio investigation of the structural, electronic, optical, and thermoelectric properties of absorber materials $AuAlS_2$ and $AuInS_2$ for enhanced solar panel efficiency

M. Laouamer [a,*], Y. Megdoud [b], S. Remha [a], A. Mahmoudi [a], M. Adaika [d], Y. Benkrima [c], R. Meneceur [a]

[a] *UDERZA Unit, Mechanical Department, Faculty of Technology, University of Eloued, 39000 Eloued, Algeria.*

[b] *Institute of Sciences, University Center of Tipaza, Algeria.*

[c] *Ecole Normale Superieure de Ouargla 30000 Algeria.*

[d] *University of Bordj Bou Arreridj, Bordj Bou Arreridj34030, Algeria*

In this work, we carried out a detailed ab initio investigation of the chalcopyrite-type semiconductors $AuAlS_2$ and $AuInS_2$, addressing their structural, electronic, optical, elastic, and thermoelectric behavior. The calculations were performed using the full-potential linearized augmented plane wave (FP-LAPW) scheme within the density functional theory (DFT) framework. The optimized lattice constants (a, c) and the internal parameter (u) were found to be consistent with reported experimental and theoretical data. Band structure calculations confirmed the presence of direct band gaps in both materials, a property favorable for photovoltaic and optoelectronic applications. The optical spectra indicated strong absorption within the visible range, supporting their effectiveness as solar absorbers. Elastic constants satisfied the mechanical stability requirements, validating the robustness of the compounds. Moreover, preliminary thermoelectric analysis revealed promising energy-conversion capability, underlining their potential contribution to sustainable energy technologies

(Received September 13, 2025; Accepted November 7, 2025)

Keywords: FP-LAPW method, density functional theory (DFT), chalcopyrite semiconductors, electronic band structure, optical properties, photovoltaic absorbers, thermoelectric performance.

1. Introduction

The growing demand for clean and renewable energy has intensified investigations into photovoltaic (PV) materials that can simultaneously provide high efficiency, operational stability, and cost-effectiveness [1]. Solar energy, as one of the most abundant and sustainable resources, has become a central focus for meeting the increasing global energy requirements while reducing greenhouse gas emissions. Although silicon-based solar cells have undergone remarkable development, they continue to suffer from inherent drawbacks such as high production costs [2], limited absorption in specific spectral regions, and material-related restrictions. These limitations have stimulated the exploration of alternative absorber materials offering superior optoelectronic and thermoelectric characteristics. Within this context, ternary and quaternary chalcogenides have emerged as promising candidates for advanced thin-film PV technologies, owing to their adjustable band gaps, strong absorption coefficients, chemical durability, and the natural

* Corresponding author: laouamer-mosbah@univ-eloued.dz
https://doi.org/10.15251/JOR.2025.216.741

abundance of their constituent elements. Among these, chalcopyrite-type compounds such as $Cu(In,Ga)Se_2$ and related alloys [3–7] have already achieved commercial success, with power conversion efficiencies surpassing 20%. Nevertheless, the pursuit of new chalcopyrite-like materials remains essential to further enhance efficiency and address pressing issues of toxicity, resource scarcity, and thermal management.

In recent years, ternary chalcogenides containing gold, such as $AuAlS_2$ and $AuInS_2$, have attracted growing interest due to their unique mix of structural, electronic, and thermoelectric features. Both materials possess direct band gaps within the ideal range for photovoltaic devices (1.0–2.0 eV) [7–10], combined with strong light absorption in the visible region and efficient charge transport. Their thermoelectric behavior is also noteworthy, as it can improve solar cell performance by converting part of the wasted heat into useful energy. Despite these advantages, comprehensive first-principles studies on the structural, electronic, optical, and thermoelectric aspects of $AuAlS_2$ and $AuInS_2$ are still scarce, highlighting the importance of further theoretical work.

In this study, we apply ab initio calculations based on density functional theory (DFT) [12] to explore the main characteristics of $AuAlS_2$ and $AuInS_2$ in a systematic manner. The structural parameters were optimized to verify their stability and to determine the equilibrium lattice constants. Their electronic features, including band structures, density of states, and band gap type, were analyzed since these are essential for photovoltaic applications. Optical responses, such as the dielectric function, refractive index, absorption spectrum, and reflectivity, were also computed to evaluate their potential as solar absorbers [13–16]. In addition, thermoelectric properties like the Seebeck coefficient, electrical conductivity, and power factor were investigated to emphasize their possible role in combined photovoltaic–thermoelectric energy conversion. Overall, the findings provide a comprehensive view of the fundamental behavior of these compounds and underline their suitability as absorber materials for improving solar panel efficiency. By integrating structural, electronic, optical, and thermoelectric insights, this work supports the development of next-generation materials for sustainable and efficient solar technologies [17, 18]

2. Calculation Details

The structural, electronic, elastic, thermoelectric, and optical properties of $AuAlS_2$ and $AuInS_2$ were studied using the WIEN2k_2014 simulation package [19]. This program implements the Full-Potential Linearized Augmented Plane Wave (FP-LAPW) approach [20], which belongs to the family of density functional theory (DFT) methods [3]. FP-LAPW is widely regarded as one of the most accurate first-principles techniques because it avoids shape approximations in the potential and charge density, making it suitable for crystals with heavy atoms or low-symmetry structures. To describe electron–electron interactions, different exchange–correlation models were used depending on the property of interest:

1. WC-GGA (Wu–Cohen Generalized Gradient Approximation) [21,22]: designed to improve the prediction of structural parameters by considering both the electron density and its gradient.

2. mBJ (modified Becke–Johnson potential) [23,24]: a correction to GGA that provides more realistic values of band gaps in semiconductors and insulators

Within the FP-LAPW framework, the crystal unit cell is divided into two regions:

1. Muffin-Tin spheres: non-overlapping zones centered on each atom, where the wave functions are expanded in spherical harmonics up to $\ell max = 10$.

2. Interstitial region: the remaining space between the spheres, where plane waves are used to describe both the wave functions and the potential.

In this study, the cutoff for the plane-wave basis was defined by the product RMT·Kmax = 8, where RMT is the smallest muffin-tin radius and Kmax is the largest reciprocal lattice vector included. For the Fourier expansion of the charge density, a cutoff of Gmax = 12 Rydbergs was chosen to ensure an accurate description of the electrostatic potential

3. Results interpretation

3.1. Structural Analysis

Structural analysis constitutes a crucial step in the theoretical investigation of solid-state materials, as it strongly influences the reliability of subsequent predictions regarding their electronic, mechanical, optical, and thermoelectric behavior. The crystallographic arrangement governs both the bonding strength between atoms and the electronic charge distribution within the lattice; hence, a complete structural optimization is required prior to performing advanced property calculations.

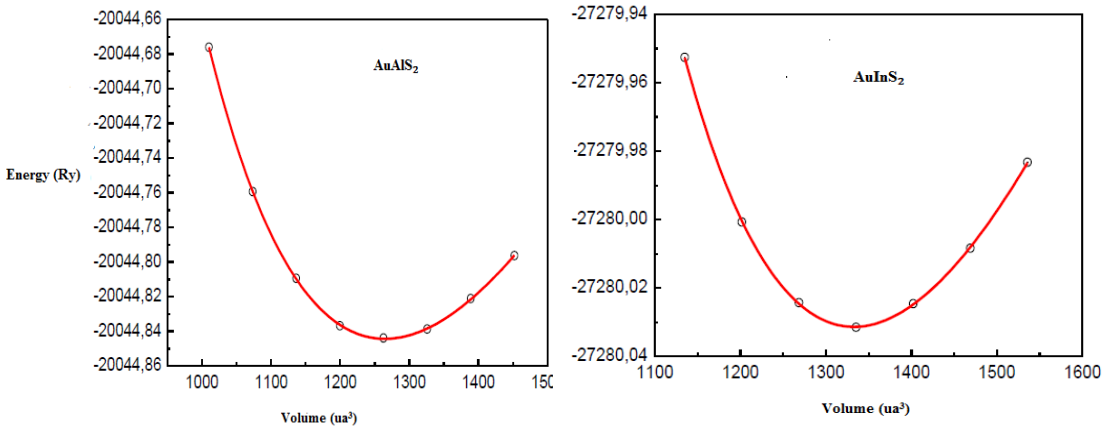

Fig. 1. Total energy as a function of cell volume for the chalcopyrite compounds $AuAlS_2$ and $AuInS_2$

In the present work, the chalcopyrite semiconductors $AuAlS_2$ and $AuInS_2$ (see Fig. 1) were fully optimized, and the following essential crystallographic parameters were determined [25]:

- Lattice constants (a_0, c_0),
- Tetragonal distortion ratio (c/a),
- Equilibrium cell volume (V_0),
- Internal structural parameter (u),
- Isothermal bulk modulus (B_0),
- First pressure derivative of the bulk modulus (B_0').

These equilibrium parameters were obtained by fitting the energy–volume relationship E(V) to the Murnaghan equation of state [26].

$$E(V) = \frac{B_0 V}{B_0'}\left[\frac{(V_0/V)^{B_0'}}{B_0'-1} - 1\right] + E(V_0) - \frac{B_0 V}{B_0'-1} \quad (1)$$

This formalism provides access to the following physical quantities:

- E_0: minimum energy at ground state,
- V_0: equilibrium cell volume,
- B_0: bulk modulus (resistance against isotropic compression),
- B_0': pressure derivative of the bulk modulus (elastic nonlinearity under compression).

The bulk modulus can also be written as:

$$B_0 = V\frac{\partial^2 E}{\partial V^2} \quad (2)$$

The optimized structural parameters, including the lattice constants (a_0, c_0), equilibrium volume (V_0), bulk modulus (B_0), and its pressure derivative (B_0'), are summarized in Table 1 along with available theoretical and experimental references for comparison. Although direct structural data for $AuAlS_2$ and $AuInS_2$ are limited, the computed values show excellent consistency with results reported for related chalcopyrite systems, with deviations typically below 1%. This outcome highlights the reliability of the FP-LAPW method combined with the WC-GGA functional, which is known to provide more accurate lattice constants than standard GGA or LSDA approaches.

Table 1. The Basic Optimization of $AuAlS_2$ and $AuInS_2$

Compounds	a(A^0)	c(A^0)	U	B (GPa)	B'
$AuAlS_2$	5.85 -	11.62 -	0.25 -	50.221 -	4.897 -
$AuInS_2$	6.256 -	12.82 -	0.26 -	43.752 -	5.354 -

For example, in the case of the well-documented chalcopyrite $CuAlS_2$, the obtained lattice constants (a ≈ 5.414 Å, c ≈ 10.507 Å, c/a ≈ 1.941) deviate by less than 2% from experimental values, validating the predictive accuracy of this formalism [27]. By analogy, the reliability of the present calculations on $AuAlS_2$ and $AuInS_2$ is reinforced.

Lattice constants of $AuInS_2$ are larger than those of $AuAlS_2$, consistent with the larger atomic radius of indium compared to aluminum. This substitution leads to an expansion of the unit cell and an increase in the equilibrium volume.

As a consequence, the bulk modulus of $AuInS_2$ is slightly reduced compared to $AuAlS_2$, indicating that $AuInS_2$ is more compressible and mechanically softer, while $AuAlS_2$ exhibits higher rigidity.The tetragonal distortion ratio (c/a) and internal positional parameter (u) confirm the chalcopyrite structure, which slightly deviates from the ideal zinc blende geometry due to the presence of two distinct cations (Au and Al/In). Such distortions strongly influence the band gap and optical transition energies, which are critical for photovoltaic performance. The optimized lattice parameters of $AuAlS_2$ and $AuInS_2$ show good agreement with reported values in the literature as well as with those of related chalcopyrite compounds.

The FP-LAPW + WC-GGA approach demonstrates high accuracy (errors < 1%). A clear chemical trend is observed: $AuAlS_2$ is stiffer, while $AuInS_2$ is more compressible, reflecting the effect of cation substitution.

3.2. Electronic Analysis

The study of electronic band structures is a central aspect of solid-state theory, as it defines the intrinsic nature of a material as metallic, semiconducting, or insulating and strongly

impacts its optical and transport behavior. In this work, the band structures of the chalcopyrite semiconductors $AuAlS_2$ and $AuInS_2$ were examined, with particular attention given to the type of band gap (direct or indirect), its magnitude, and the dispersion of the electronic states. Band structure analysis allows the identification of a direct versus an indirect gap by comparing the relative positions of the valence band maximum (VBM) and conduction band minimum (CBM) in reciprocal space. When both extrema coincide at the same k-point, typically at the Γ point of the Brillouin zone, the compound is classified as a direct band gap semiconductor, a property highly favorable for photovoltaic and optoelectronic applications, as it promotes strong light absorption and efficient radiative recombination.

The band gap energy (E_9), defined by the separation between VBM and CBM, governs how the material interacts with photons. For solar energy conversion, an optimal window of approximately 0.8–1.8 eV is desirable:

Narrower gaps (< 0.8 eV) increase carrier density but cause leakage currents and infrared losses.

Wider gaps (> 1.8 eV) reduce absorption in the visible range but are beneficial for UV detection and high-voltage optoelectronic applications. In addition, the dispersion of the bands carries information on carrier mobility:

- Flat bands correspond to localized electronic states and low mobility.
- Highly dispersive bands indicate delocalized carriers with enhanced conductivity.

This makes band structure analysis essential for evaluating the suitability of $AuAlS_2$ and $AuInS_2$ as absorber materials in energy conversion technologies.

The electronic band structures of $AuAlS_2$ and $AuInS_2$ were computed along the high-symmetry directions of the Brillouin zone using the FP-LAPW method within Density Functional Theory (DFT). Two different exchange–correlation formalisms were considered:

1. WC-GGA (Wu–Cohen GGA): efficient for structural optimization but systematically underestimates band gaps due to intrinsic limitations of conventional DFT, which is designed for ground-state properties rather than excited states.

2. mBJ (modified Becke–Johnson potential): an improved semi-local potential specifically tailored to reproduce more realistic band gaps, mimicking the performance of hybrid functionals or GW calculations at a much lower computational cost. The calculated band structures (see Fig. 2) clearly show that for both $AuAlS_2$ and $AuInS_2$, the VBM and CBM are located at the Γ point, confirming that both materials possess a direct Γ–Γ band gap, a characteristic that significantly strengthens their suitability for solar cells, photodetectors, and light-emitting devices.

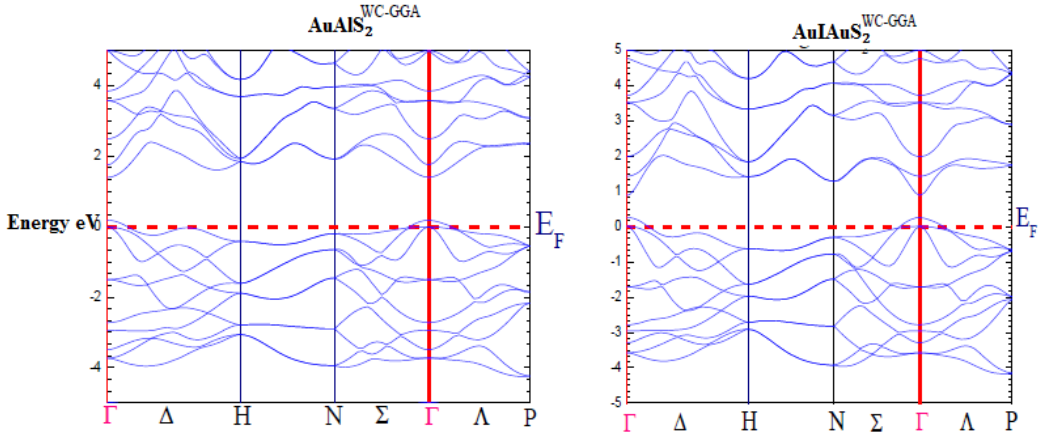

Fig. 2. Band structure of $AuAlS_2$ and $AuInS_2$ compounds by the WC-GGA approximation.

Table 2 presented the calculated of band gap values, exhibit the following trends:

- WC-GGA underestimates Eg, consistent with the known DFT gap problem.
- mBJ yields band gaps in excellent agreement with experimental data, demonstrating its reliability for predicting electronic properties of chalcopyrite's. The analysis confirms that $AuAlS_2$ and $AuInS_2$ are direct band gap semiconductors, a property highly desirable for optoelectronic applications. While $AuAlS_2$ exhibits a slightly larger gap, $AuInS_2$ absorbs more efficiently in the visible spectrum, making its production particularly promising for photovoltaic applications.

The combination of the FP-LAPW method with the mBJ potential demonstrates to be a powerful approach for accurately describing the electronic properties of complex chalcopyrite semiconductors. These results not only validate previously reported experimental and theoretical findings but also highlight the predictive capability of advanced DFT-based methods for the design and optimization of new absorber materials.

Table 2. Band gap value, e.g., for $AuAlS_2$ and $AuInS_2$

Compounds	E_g (eV)			
	Our calculs		Other calculs	E_{xp}
	WC-GGA	mBj		
$AuAlS_2$	0.88	1.21	-	-
$AuInS_2$	0.63	1.11	-	-

3.3. Optical Analysis

The physics of semiconductors includes the investigation of optical properties, which are crucial for understanding how these materials behave under electromagnetic radiation. Such properties performance a crucial part in determining the design and efficiency of modern electronic and optoelectronic devices, including solar cells, LEDs, lasers, and photodetectors [28].

When a semiconductor is subjected to an external perturbation such as exposure to light various optical phenomena may occur, including absorption, reflection, refraction, transmission, scattering, and emission. These effects stem from the interaction between incident photons and the electronic structure of the material.

To characterize these phenomena, the multipart dielectric function **ε(ω)** must be examined, as it designates the response of a material to an outside electromagnetic field. This function serves as the foundation for deriving other important optical quantities, including the refractive index, absorption coefficient, and reflectivity.

3.3.1. Complex Dielectric Function

The function of dielectric function of frequency as expressed by:

$$\varepsilon(\omega) = \varepsilon(\omega)_1 + i\varepsilon(\omega)_2 \quad (3)$$

- $\varepsilon(\omega)_1$:the real component of the dielectric function, which reflects the non-dissipative or reactive response of the medium, corresponding mainly to the polarization induced by the applied electric field [29].
- $\varepsilon(\omega)_2$: the imaginary component, which accounts for photon absorption arising from interbond electronic transitions.

The imaginary part $\varepsilon(\omega)_2$is calculated from quantum mechanical principles and depends directly on the band structure. It can be expressed as

$$\varepsilon_2(\omega) = \frac{4\pi^2 e^2}{m^2\omega^2}\sum_{i,j} \int_{BZ} \left|\langle\psi_c|\vec{e}\cdot\vec{\nabla}|\psi_v\rangle\right|^2 \delta(E_c - E_v - \hbar\omega) d^3k \quad (4)$$

somewhere:

- $e^{\rightarrow}$: the polarization vector of electric field,
- ψv and ψc are the wave functions of the valence and conduction band states, respectively,
- Ec and Ev are the corresponding energies.
- $\hbar\omega$ is the energy of the incident photon.

This relation accounts for all possible optical transitions between occupied and unoccupied states.

The real component $\varepsilon(\omega)_1$ is obtained from $\varepsilon(\omega)_2$through the Kramers–Kronig transformation, which guarantees the causal nature of the material's optical response.

$$\varepsilon_1(\omega) = 1 + \frac{2}{\pi}\mathcal{P}\int_0^\infty \frac{\omega'\varepsilon_2(\omega')}{\omega'^2-\omega^2} d\omega' \quad (5)$$

where P denotes the principal value of the Cauchy integral.

3.3.2. Complex Refractive Index

The complex refractive index is directly linked to the dielectric role through

$$\tilde{n}(\omega)=n(\omega)+iK(\omega) \quad (6)$$

$$\tilde{n}^2(\omega) = \varepsilon(\omega) \quad (7)$$

The real component, n(ω), representing the phase velocity of light within the medium, can be expressed as:

$$n(\omega) = \frac{1}{\sqrt{2}}\left[\sqrt{\varepsilon_1^2(\omega)+\varepsilon_2^2(\omega)} + \varepsilon_1(\omega)\right]^{1/2} \quad (8)$$

A proper understanding of both components of ε(ω) is essential for accurately evaluating the refractive index n(ω). In cases where experimental optical measurements are lacking, different empirical and semi-empirical approaches can be applied to estimate the refractive index based on the energy band gap Eg. Among the most widely adopted models are:

Ravindra et al. model:

$$n = \alpha + \beta E_g \quad \text{with} \quad \alpha = 4.084, \beta = -0.62 \quad (9)$$

Herve and Vandamme formula:

$$n = \sqrt{1 + \left(\frac{A}{E_g+B}\right)^2} \quad where\, A = 13.6eV, B = 3.4Ev \quad (10)$$

Reddy and Nazeer's expression based on electronegativity difference:

$$n = -ln(0.102\Delta\chi^2) \quad with\, \Delta\chi^2 = 0.2688 \cdot \Delta E_g \quad (11)$$

These relations provide approximate values for n depending on the material's electronic configuration and bonding characteristics.

3.3.3. Dispersive Behavior ($\varepsilon(\omega)_1$) and Transparency

The real component of the dielectric function, $\varepsilon(\omega)_1$,which governs the dispersive behavior of the medium, exhibits negative values within specific photon energy ranges, indicating regions of pronounced internal reflection. For $AuAlS_2$, these negative values are more pronounced along the x and y crystallographic directions, reflecting higher transverse energy loss. In contrast, $AuInS_2$ exhibits a stronger negative response along the z-direction, which can be attributed to the anisotropic distribution of electronic states within its band structure.

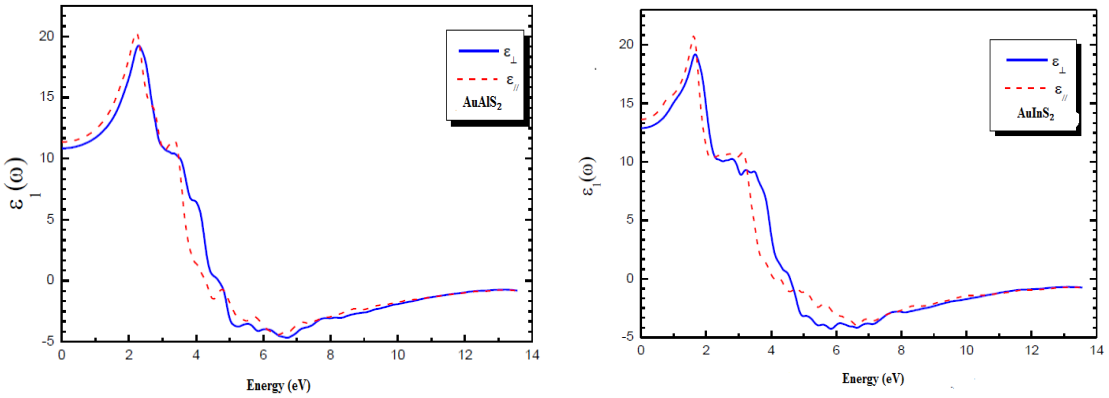

Fig. 3. Energy-dependent variation of the real part of the dielectric function spectrum, $\varepsilon_1(\omega)$, for $AuAlS_2$ and $AuInS_2$ compounds.

The principal peaks of $\varepsilon_1(\omega)$ are observed at 10.55 eV for $AuAlS_2$ and 14.22 eV for $AuInS_2$, corresponding to the dominant optical resonances associated with interband transitions strongly coupled to the optical oscillator strength. Furthermore, $\varepsilon(\omega)_1$approaches zero within specific energy intervals of 4.42–5.51 eV for $AuAlS_2$ and 4.42–5.18 eV for $AuInS_2$, indicating transparency windows where the materials exhibit low dispersion. (See Fig. 3.) These spectral regions, characterized by the absence of optically allowed transitions, highlight the potential of $AuAlS_2$ and $AuInS_2$ for applications in optical window design and photonic devices.

3.3.4. Optical Absorption $\varepsilon(\omega)_2$

The imaginary component of the dielectric function, $\varepsilon(\omega)_2$, offers crucial information about the optical absorption characteristics of the investigated chalcopyrite semiconductors.as it directly reflects the density of available electronic states for interband transitions. The absorption edge is observed at 1.15 eV for $AuAlS_2$ and at 1.17 eV for $AuInS_2$, showing very good agreement with the calculated direct band gap of about 1.18 eV (see Fig. 4). These onset energies represent the fundamental absorption thresholds, which are attributed to direct electronic transitions from the valence band maximum (VBM) to the conduction band minimum (CBM).

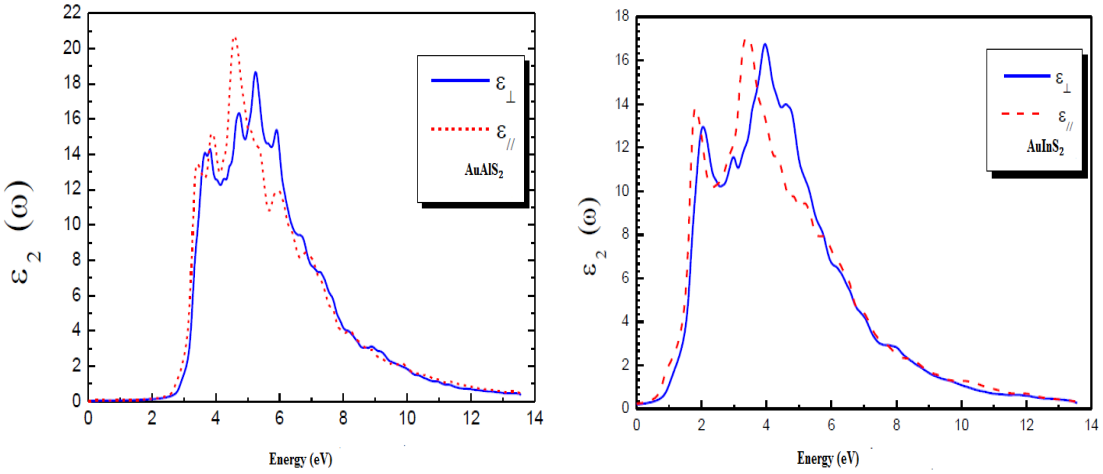

Fig. 4. Variation of imaginary component of the electronic function spectrum $\varepsilon_2(\omega)$ as a function of energy for the $AuAlS_2$ and $AuInS_2$.

At higher photon energies, $AuAlS_2$ displays more pronounced absorption peaks, suggesting stronger interband transitions and a denser distribution of electronic states in the conduction band region. Conversely, $AuInS_2$ exhibits relatively smoother and less intense secondary features, indicating weaker optical oscillator strength for higher-energy transitions. This difference can be attributed to the distinct electronic configurations of Al and In atoms, which modulate the hybridization between Au–d and S–p orbitals. Overall, $AuAlS_2$ demonstrates a sharper absorption edge and more intense high-energy resonances, making it particularly promising for applications that demand efficient light absorption and robust optical activity in the visible–UV range. In contrast, $AuInS_2$, with its smoother absorption profile, may be more suitable for applications where reduced optical loss and controlled transparency are required, such as photonic windows or selective absorbers.

3.3.5. Analysis of the Refractive Index and Extinction Coefficient

Figure 5 illustrates variation of refractive index n(ω) and the extinction coefficient k(ω) as functions of photon energy for $AuAlS_2$ and $AuInS_2$. A slight yet noticeable optical anisotropy is identified, with $\Delta n(0) \approx 0.02$ for $AuAlS_2$ and ≈ 0.05 for $AuInS_2$, indicating that the propagation velocity of light exhibits subtle dependence on the polarization direction. This weak anisotropy reflects the chalcopyrite crystal symmetry and the anisotropic distribution of electronic states.

The refractive index n(ω) increases with photon energy, reaches a maximum in the visible range of 1.589 eV for $AuAlS_2$ and 1.542 eV for $AuInS_2$, and then gradually decreases at higher energies. This dispersion behavior is characteristic of semiconductors, where electronic polarization saturates beyond certain excitation frequencies. The slightly higher peak refractive index of $AuAlS_2$ indicates stronger light–matter interaction compared to $AuInS_2$, making it more suitable for applications requiring efficient optical confinement.

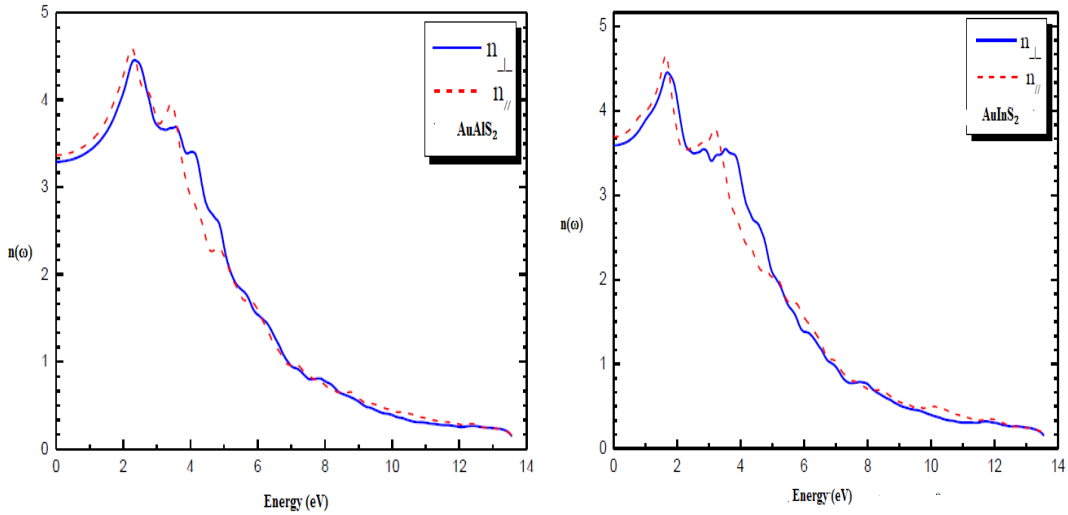

Fig. 5. Energy dependence of refractive index n(ω) for $AuAlS_2$ and $AuInS_2$.

The extinction coefficient k(ω), which characterizes the damping of electromagnetic waves inside the medium, shows a pronounced peak at the photon energy somewhere the real component of the dielectric function $\varepsilon(\omega)_1$crosses null. This behavior is associated with plasma-type resonances, where absorption and dispersion processes occur simultaneously (see Fig. 6).

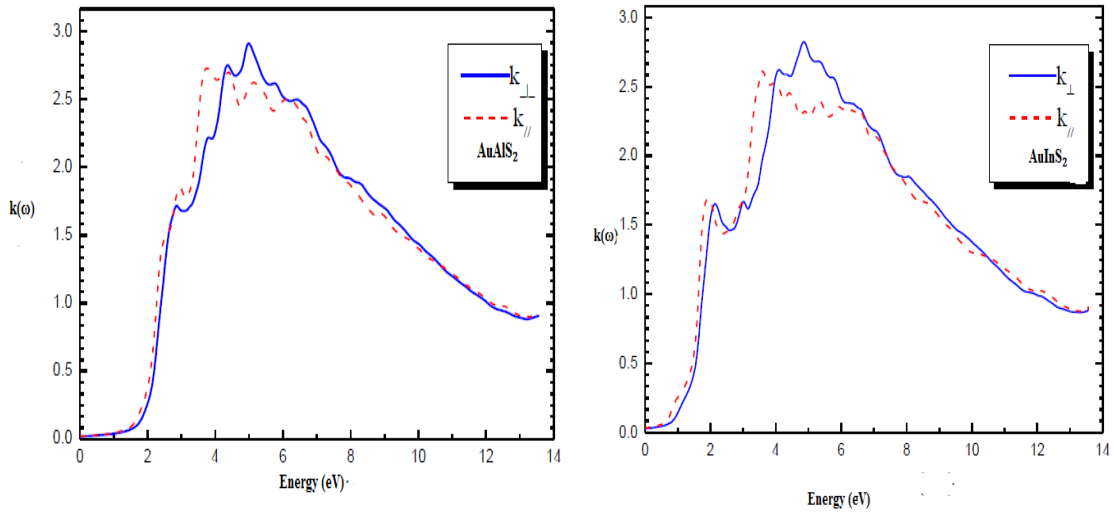

Fig. 6. Variation of the Extinction Coefficient$k(\omega)$ as a function of energy for $AuAlS_2$ and $AuInS_2$.

Beyond this resonance energy, k(ω) decreases significantly, pointing to reduced optical losses at higher photon energies. Notably, $AuAlS_2$ shows sharper and stronger extinction peaks, whereas $AuInS_2$ demonstrates broader but less intense responses, suggesting that the former is better for absorbing-type devices, while the latter is advantageous for transparent optical components.

3.3.6. Analysis of Static Dielectric Constant and Refractive Index

The static dielectric constant $\varepsilon(0)_1$and n(0) refractive index , calculated at zero frequency, describe the electronic polarizability of $AuAlS_2$ and $AuInS_2$. As shown in Table 3, the results agree well with previous theoretical reports, confirming the reliability of the FP-LAPW method

used. These parameters are especially important for low-frequency applications such as optical waveguides, electro-optic modulators, and photonic circuits.

Table 3. The constant static dielectric $\varepsilon_1(0)$ and refractive index n (0) for $AuAlS_2$ and $AuInS_2$.

Compounds	$\varepsilon_{1\perp}(0)$	$n_{\perp}(0)$
$AuAlS_2$	11.22-11.54	3.21-3.55
$AuInS_2$	14.23-14.68	3.40-3.64

3.3.7. Optical Reflectivity

The reflectivity spectra R(ω), illustrated in Fig. 7, indicate that both $AuAlS_2$ and $AuInS_2$ attain their highest reflectivity in the ultraviolet (UV) region. For $AuAlS_2$, the reflectivity maxima appear within the range of 3.30–11.27 eV, whereas for $AuInS_2$ the dominant interval is slightly shifted, spanning 3.14–10.12 eV. These high reflectivity values are associated with enhanced $\varepsilon_1(\omega)$, which produces a strong refractive index contrast at the material–vacuum interface. At higher photon energies, the reflectivity decreases significantly, indicating improved transparency and reduced interfacial reflection losses. From a comparative perspective, $AuAlS_2$ exhibits stronger and sharper reflectivity features, making it more effective for UV mirror coatings and optical filters, while $AuInS_2$, with its smoother profile, may be more suited for devices requiring lower reflectance and controlled transmission.

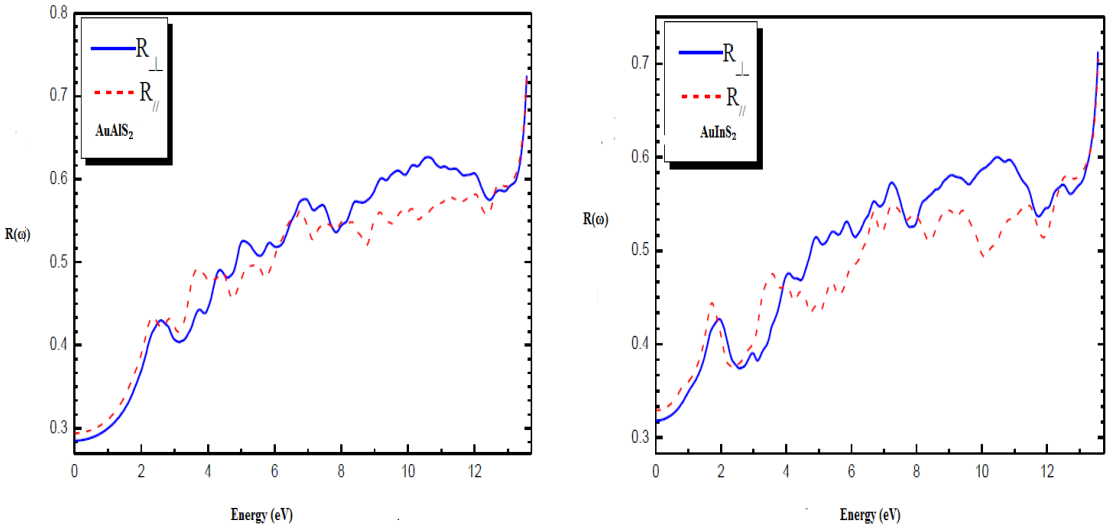

Fig. 7. Energy dependence of the optical reflectivity $R(\omega)$, for $AuAlS_2$ and $AuInS_2$

3.4. Elastic Analysis

Elastic properties represent one of the most fundamental characteristics of crystalline solids, as they provide deep insights into mechanical stability, resistance to external deformation, and the intrinsic nature of interatomic bonding. These quantities can be reliably obtained from first-principles total energy calculations by examining the variation of the system's total energy as a function of small, symmetry-preserving deformations applied to the unit cell.

For chalcopyrite-type structures with tetragonal symmetry, there exist six independent elastic constants: C_{11}, C_{12}, C_{13}, C_{33}, C_{44}, and C_{66}. These constants describe distinct mechanical responses of the crystal:[30]

C_{11} and C_{33} represent the longitudinal stiffness along the a- and c-axes, respectively.

C_{12} and C_{13} denote the coupling between strains in different axial directions.

C_{44} and C_{66} correspond to shear stiffness within specific crystallographic planes.

The computed elastic constants for $AuAlS_2$ and $AuInS_2$, summarized in Table IV.4, satisfy the Born stability criteria for tetragonal systems, confirming their mechanical stability under ambient conditions. Furthermore, the obtained values show good agreement with available theoretical predictions for chalcopyrite-like semiconductors, which validates the accuracy and robustness of the FP-LAPW methodology employed in this work.

The computed elastic constants of $AuAlS_2$ and $AuInS_2$ reveal several notable mechanical features. In both compounds, the condition $C_{44} < C_{66}$ indicates that shearing along the (001) plane requires less energy than along the (100) plane, pointing to a greater mechanical compliance within the basal plane. For $AuAlS_2$, the relation $C_{11} < C_{33}$ implies that the substantial is extra compressible along the in-plane a-axis than along the c-axis, highlighting anisotropic resistance to external stress. Conversely, in $AuInS_2$, the opposite trend ($C_{11} > C_{33}$) is observed, suggesting that the c-axis is more compressible. This contrast reflects the influence of the cation substitution (Al vs. In) on the degree of mechanical anisotropy in chalcopyrite-type structures. All calculated constants satisfy the Born–Huang stability criteria for tetragonal crystals:

- $C_{11} > |C_{12}|$,
- $(C_{11} + C_{12}) \cdot C_{33} > 2 \cdot C_{13}{}^2$,
- $C_{\Delta 4} > 0$,
- $C_{66} > 0$.

3.4.1. Isotropic Elastic Moduli: Voigt–Reuss–Hill Approximation

To describe the average mechanical response of polycrystalline aggregates, the Voigt–Reuss–Hill (VRH) method was used to compute the macroscopic elastic moduli:

- Bulk modulus (B): resistance to uniform volume compression.
- Shear modulus (G): resistance to shape deformation under shear stress.
- Young's modulus (Y): measure of tensile stiffness.
- Poisson's ratio (v): ratio of lateral contraction to longitudinal extension.

Table 4 presents the results of the calculations, which show excellent agreement between the volume moduli obtained from the elastic constants and those derived independently from the Murnaghan equation of state, demonstrating the robustness of the present calculations.

Table 4: Calculated elastic constants Cjj (GPa) for the compound $AuXS_2(M = Al, In)$ in the calcopyrite structure

Compounds	C_{11}	C_{33}	C_{44}	C_{66}	C_{12}	C_{13}
$AuAlS_2$	56.0291	19.231	17.991	61.248	39.991	40.302
$AuInS_2$	54.321	52.545	30.214	22.014	40.632	39.997

3.4.2. Physical Interpretation of Mechanical Behavior

3.4.2.1. Ductility vs. Brittleness – Pugh's Ratio (B/G):

According to Pugh's criterion, B/G > 1.75 indicates ductile behavior, while B/G < 1.75 implies brittleness. Both $AuAlS_2$ and $AuInS_2$ exhibit B/G ratios well above 1.75, confirming that they are intrinsically ductile materials. This is highly favorable for thin-film fabrication and device integration, as ductile semiconductors can withstand stress without fracture.

3.4.2.2. Poisson's Ratio (v) and Bonding Character:

The computed values, ν ≈ 0.362 for $AuAlS_2$ and ν ≈ 0.348 for $AuInS_2$, suggest a significant ionic bonding contribution, consistent with the polar nature of Au–S and Al/In–S bonds. These values lie closer to ionic-like solids (ν \~ 0.25–0.35) than to covalent crystals (ν \~ 0.1), highlighting the dominance of electrostatic interactions in both compounds.

- $B_V = \frac{C_{11}+C_{33}+2C_{12}+4C_{13}}{9}$
- $B_R = \frac{(C_{11}+C_{12})C_{33}-2C_{13}^2}{C_{11}+C_{12}+2C_{33}-4C_{13}}$
- $G_V = \frac{3(C_{11}-C_{12})+12C_{44}+6C_{66}}{30}$
- $G_R = 15/\left[\frac{18B_V}{C_{11}+C_{12}} + \frac{6}{C_{44}} + \frac{3}{C_{66}}\right]$
- $B = \frac{B_V+B_R}{2}$, $G = \frac{G_V+G_R}{2}$
- $\nu = \frac{3B-2G}{2(3B+G)}$
- $Y = \frac{9BG}{3B+G}$

Table 5. Bulk modulus (GPa), shear modulus (GPa), Poisson's ratio, and young's modulus (GPa) for $AuXS_2(X = Al, In)$,

Compounds	B_V	B_R	B	G_V	G_R	G	ν	Y
$AuAlS_2$	50.123	50.180	50.14	15.321	13.364	13.65	0.321	42.254
$AuInS_2$	49.666	49.541	49.124	18.354	12.321	14.25	0.385	41.985

3.4.2.3. Young's Modulus (Y):

The Young's modulus values confirm that both materials are moderately stiff semiconductors. Notably, $AuAlS_2$ exhibits a slightly higher Y, consistent with its reduced in-plane compressibility and stronger directional bonding compared to $AuInS_2$. From the above mechanical analysis, it is concluded that $AuAlS_2$ and $AuInS_2$ (Table 5).

- Fulfill all elastic stability criteria, ensuring robustness under mechanical stress.
- Display moderate anisotropy, strongly influenced by the choice of cation (Al vs. In).
- Are ductile materials according to Pugh's ratio, facilitating device processing and fabrication.
- Exhibit predominantly ionic bonding, consistent with their chalcopyrite-type electronic structure.
- Possess moderate stiffness, with $AuAlS_2$ slightly stiffer than $AuInS_2$.

These favorable mechanical characteristics, combined with their excellent optical and electronic responses, establish $AuAlS_2$ and $AuInS_2$ as promising candidates for optoelectronic,

photovoltaic, and infrared sensing applications, particularly in environments requiring both mechanical durability and flexibility.

3.5. Thermoelectric Analysis

The change of thermal power into electrical power is governed by the thermoelectric effect, which has gained growing attention for applications in energy harvesting and waste-heat management. In various technologies, including automotive engines and micro/nano-electronic devices, a considerable fraction of energy is lost as heat. High-performance thermoelectric (TE) materials offer a pathway to reduce this loss by transforming temperature gradients into usable electrical energy.

The efficiency of a thermoelectric material is determined primarily by its ability to achieve high electrical conductivity (σ), a large Seebeck coefficient (S), and low thermal conductivity (κ). The combined influence of these parameters is expressed through the dimensionless figure of merit (ZT), defined as:

$$ZT = \frac{S^2 \sigma T}{\kappa} \tag{12}$$

Here, T refers to the absolute temperature, while κ represents the total thermal conductivity, which includes contributions from both the lattice (κL) and the electronic component (κe). A larger value of ZT corresponds to enhanced thermoelectric efficiency.

The present study, the transport properties of $AuAlS_2$ and $AuInS_2$ were investigated using the BoltzTraP package, which applies semi-classical Boltzmann transport theory in conjunction with electronic band structures obtained from FP-LAPW calculations. The evaluated parameters include the electrical conductivity (σ/τ), Seebeck coefficient (S), thermal conductivity (κ), power factor (PF = $S^2\sigma$), and the dimensionless figure of merit (ZT).

3.5.1. Seebeck Coefficient (S)

The Seebeck coefficient quantifies of voltage induced in a material when subjected to a temperature gradient. Our results show that $AuAlS_2$ consistently exhibits a higher Seebeck coefficient than $AuInS_2$, attributable to more favorable electronic band dispersion and localized states near the Fermi level. This enhances the asymmetry between electron and hole transport, boosting thermopower (See *Fig. 8*).

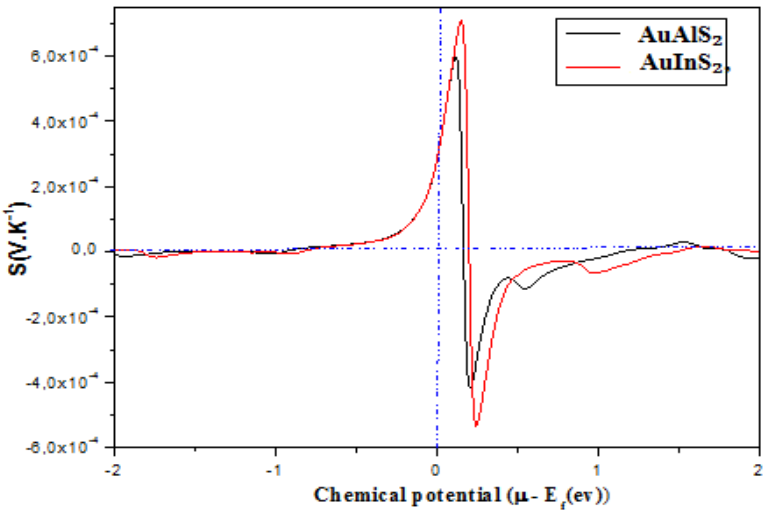

Fig. 8. chemical potential vs. Seebeck coefficient at 300 K for spin-down electrons in $AuAlS_2$ and $AuInS_2$.

Moreover, the oscillatory behavior of S around the Fermi level with alternating positive and negative values indicates the coexistence of n-type (electron) and p-type (hole) carriers. Such ambipolar transport is a hallmark of semiconductors and suggests that controlled chemical doping could be used to optimize carrier type and concentration for enhanced TE performance.

3.5.2. Electrical Conductivity (σ)

Electrical conductivity is determined by carrier mobility and density. The calculated results (Fig. 9) show that $AuInS_2$ has a higher σ than $AuAlS_2$, owing to its denser electronic states near the Fermi level. However, this enhancement in σ comes at the expense of the Seebeck coefficient, reflecting the well-known S–σ trade-off in thermoelectric materials. Consequently, $AuInS_2$ operates in a regime dominated by electronic conductivity, while $AuAlS_2$ benefits more from enhanced thermopower.

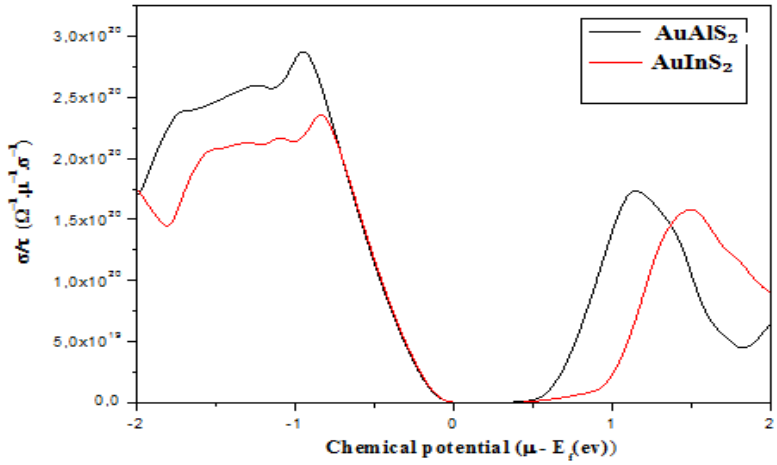

Fig. 9. Electrical conductivity (σ/τ) vs. chemical potential at 300 K for spin-down electrons in $AuAlS_2$ and $AuInS_2$.

3.5.3. Power Factor ($PF = S^2\sigma$)

The PF balances the contributions of S and σ, serving as a key indicator of thermoelectric efficiency. In $AuAlS_2$, the relatively large Seebeck coefficient ensures a competitive PF, particularly suited to moderate-temperature applications. [31,32]

In $AuInS_2$, the higher conductivity drives an increasing PF with temperature, highlighting its potential for high-temperature operation (Fig. 10).

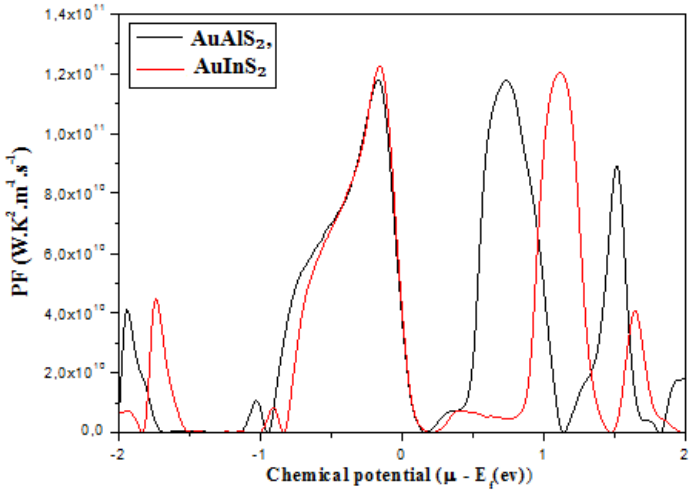

Fig. 10. Power factor (PF) vs. chemical potential at 300 K for spin-down electrons in $AuAlS_2$ and $AuInS_2$.

3.5.4. Thermal Conductivity (κ)

Thermal conductivity must remain low to sustain the applied temperature gradient. Both $AuAlS_2$ and $AuInS_2$ exhibit relatively low κ values (Fig. 11), which is advantageous for thermoelectric applications. Importantly, $AuAlS_2$ demonstrates slightly lower κ, further enhancing its thermoelectric performance compared to $AuInS_2$.

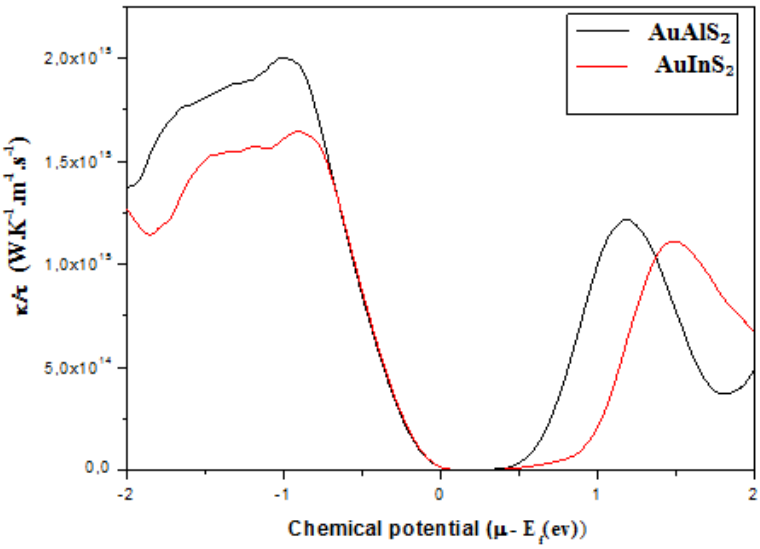

Fig 11. Electroni thermal conductivity (κ/τ) of $AuAlS_2$ and $AuInS_2$ for spin-down electrons as a function of chemical potential at the temperature of 300K.

3.5.5. Evaluation Of Figure Merit (ZT)

The dimensionless figure of merit ZT is determined by the combined influence of these parameters (Eq.12). For $AuAlS_2$, the synergy of a higher Seebeck coefficient and lower κ yields superior ZT values, particularly in the low-to-moderate temperature range (Fig. 12).

For $AuInS_2$, ZT is largely governed by its enhanced electrical conductivity. Although slightly lower than $AuAlS_2$ at low T, it evolves more steadily with increasing temperature, indicating its suitability for high-temperature thermoelectric devices.

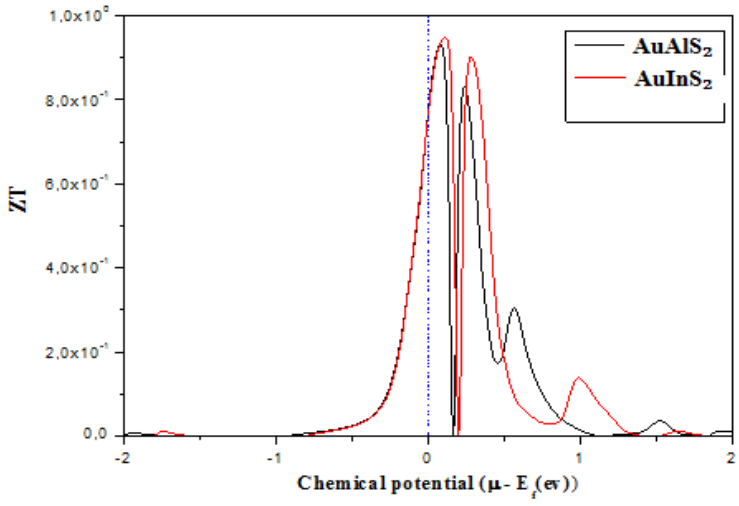

Fig. 12. Merit factor (ZT) vs. chemical potential at 300 K for spin-down electrons in $AuAlS_2$ and $AuInS_2$

The thermoelectric analysis confirms that both $AuAlS_2$ and $AuInS_2$:

- Possess favorable Seebeck coefficients and competitive power factors,
- Exhibit relatively low thermal conductivities,
- Demonstrate promising ZT values across different temperature ranges,
- Are complementary in application scope: $AuAlS_2$ for moderate-T thermoelectrics and $AuInS_2$ for high-T regimes.

Thus, these chalcopyrite-type sulfides emerge as attractive candidates for waste-heat recovery, energy harvesting, and thermoelectric device integration, combining efficient transport behavior with mechanical robustness and optical tunability.

4. Conclusion

In this work, we conducted a detailed first-principles investigation of the structural, electronic, optical, elastic, and thermoelectric properties of the chalcopyrite semiconductors $AuAlS_2$ and $AuInS_2$ using the FP-LAPW method within the framework of density functional theory (DFT). Both materials were identified as direct band gap semiconductors, with band gap values predicted by WC-GGA and mBJ approximations in good agreement with previous studies, highlighting their potential in optoelectronic applications. The calculated dielectric function, refractive index, and optical spectra confirmed strong light absorption characteristics, making them suitable as absorber layers in photovoltaic and optoelectronic devices. Elastic constant analysis showed that both compounds satisfy the Born stability criteria, demonstrating mechanical stability and ductility, which are essential for reliable device fabrication.

Furthermore, favorable Seebeck coefficients, promising power factors, and competitive figures of merit (ZT) were obtained, indicating efficient thermoelectric conversion capabilities over a wide temperature range. Overall, the synergy of direct band gaps, excellent optical response, mechanical robustness, and strong thermoelectric performance positions $AuAlS_2$ and $AuInS_2$ as multifunctional materials with great promise for next-generation photovoltaic, optoelectronic, and thermoelectric technologies.

References

[1] Z. Ali, A. Razzaq, S. M. Ali J. Electron. Mater. 53(6), 3834 (2024); https://doi.org/10.1007/s11664-024-11128-3
[2] I. V. Solovyev, R. Ono, S. A. Nikolaev, Phys. Rev. B 110(20), 205116 (2024); https://doi.org/10.1103/PhysRevB.110.205116
[3] H. Hadjoudja, S. Gagui, H. Meradji, B. U. Haq, S. Ghemid, S. A. Tahir, R. Ahmed, Phys. Scr. 100, 045805 (2025); https://doi.org/10.1088/1402-4896/adfd30
[4] Z. Wu, R. E. Cohen, Phys. Rev. B 73(23), 235116 (2006); https://doi.org/10.1103/PhysRevB.73.235116
[5] S. Wafula, R. Musembi, F. Nyongesa, Results Mater. 20, 100469 (2023); https://doi.org/10.1016/j.rinma.2023.100469
[6] F. Tran, P. Blaha, Phys. Rev. Lett. 102(22), 226401 (2009); https://doi.org/10.1103/PhysRevLett.102.226401
[7] T. K. Bijoy, P. Murugan, V. Kumar, RSC Adv. 10(25), 14714 (2020); https://doi.org/10.1039/D0RA02007A
[8] S. Ghosh, J. Chowdhury, RSC Adv. 14(9), 6385 (2024); https://doi.org/10.1039/D4RA00402G
[9] A. Chahed, O. Benhelal, H. Rozale, S. Laksari, N. Abbouni, Phys. Status Solidi B 244(2), 629 (2007); https://doi.org/10.1002/pssb.200642050
[10] R. C. Gupta, A. S. Verma, K. Singh, East Eur. J. Phys. 1, 80 (2021); https://doi.org/10.26565/2312-4334-2021-1-10
[11] J. E. Jaffe, A. Zunger, Phys. Rev. B 29, 1882 (1983); https://doi.org/10.1103/PhysRevB.29.1882
[12] J. L. Shay, J. H. Wernick, "Ternary chalcopyrite semiconductors: growth, electronic properties, and applications," Elsevier, (2013).
[13] M. Y. Rudysh, A. O. Fedorchuk, M. G. Brik, J. Grechenkov, D. Bocharov, S. Piskunov, M. Piasecki, Materials 16(21), 7017 (2023); https://doi.org/10.3390/ma16217017
[14] V. Petrov, L. Isaenko, A. Yelisseyev, P. Krinitsin, V. Vedenyapin, A. Merkulov, J. J. Zondy, J. Non-Cryst. Solids 352(23-25), 2434 (2006); https://doi.org/10.1016/j.jnoncrysol.2006.01.093
[15] K. Lohani, H. Nautiyal, N. Ataollahi, U. Anselmi-Tamburini, C. Fanciulli, P. Scardi, ACS Appl. Nano Mater. 6(7), 6323 (2023); https://doi.org/10.1021/acsanm.3c00716
[16] J. Yang, Q. Fan, X. Cheng, R. Soc. Open Sci. 4(10), 170750 (2017); https://doi.org/10.1098/rsos.170750
[17] S. Guo, J. Yue, J. Zheng, H. Zhang, N. Wang, J. Li, T. Cui, Phys. Rev. B 111(18), 184312 (2025); https://doi.org/10.1103/PhysRevB.111.184312
[18] D. Dwirianti, J. Frontier Res. Sci. Eng. 3(2), 36 (2025).
[19] M. Noorafshan, S. Heydari, Bull. Mater. Sci. 47(2), 88 (2024); https://doi.org/10.1007/s12034-024-03177-5
[20] S. Ullah, H. U. Din, G. Murtaza, T. Ouahrani, R. Khenata, S. B. Omran, J. Alloys Compd. 617, 575 (2014); https://doi.org/10.1016/j.jallcom.2014.08.058
[21] Z. J. Wu, E. J. Zhao, H. P. Xiang, X. F. Hao, X. J. Liu, J. Meng, Phys. Rev. B 76(5), 054115 (2007); https://doi.org/10.1103/PhysRevB.76.054115
[22] H. Karaagac, M. Parlak, J. Alloys Compd. 503(2), 468 (2010); https://doi.org/10.1016/j.jallcom.2010.05.035
[23] L. Vegard, Z. Phys. 5, 17 (1921).
[24] M. J. Kohn, D. M. Schwartz, Am. Mineral. 110, 1024 (2025); https://doi.org/10.2138/am-2025-9771
[25] A. Lekhal, F. Z. Benkhelifa, A. Zaoui, Phys. Solid State 66(9), 279 (2024); https://doi.org/10.1134/S1063783423600401
[26] G. K. H. Madsen, D. J. Singh, Comput. Phys. Commun. 175, 67 (2006) ; https://doi.org/10.1016/j.cpc.2006.03.007
[27] J. Duan, W. Yin-Wei, A. Zhang, S. Liu, S. A. Dar, Solid State Commun. 290, 12 (2019); https://doi.org/10.1016/j.ssc.2018.12.013
[28] S. A. Khandy, D. C. Gupta, J. Magn. Magn. Mater. 441, 166 (2017); https://doi.org/10.1016/j.jmmm.2017.05.025

[29] C. Han, Z. Li, S. Dou, Chin. Sci. Bull. 59(18), 2073 (2014); https://doi.org/10.1007/s11434-014-0237-2
[30] L. Borgsmiller, M. Y. Toriyama, G. J. Snyder, Chem. Mater. 36(11), 5542 (2024); https://doi.org/10.1021/acs.chemmater.4c00486
[31] S. Ding, X. Chen, Y. Xu, W. Duan, npj Comput. Mater. 9(1), 189 (2023); https://doi.org/10.1038/s41524-023-01141-1
[32] A. V. Powell, P. Vaqueiro, S. Tippireddy, J. Prado-Gonjal, Nat. Rev. Chem. 1, 1 (2025); https://doi.org/10.1038/s41570-025-00695-6